Chinese Journal of
POLYMER SCIENCE

RESEARCH ARTICLE

https://doi.org/10.1007/s10118-025-3276-z
Chinese J. Polym. Sci. **2025**, *43*, 588–596

Soft Crawling and Flipping Robots Based on Liquid Metal-Liquid Crystal Elastomer Composites

Ling-Xin Yuan[a], Chang-Yue Liu[a], Ji-Ping Yang[a*], and Zhi-Jian Wang[a,b*]

[a] *Key Laboratory of Aerospace Advanced Materials and Performance, Ministry of Education, School of Materials Science and Engineering, Beihang University, Beijing 100191, China*
[b] *Tianmushan Laboratory, Hangzhou 310023, China*

Electronic Supplementary Information

Abstract Soft robots have shown great advantages with simple structure, high degree of freedom, continuous deformation, and benign human-machine interaction. In the past decades, a variety of soft robots, including crawling, jumping, swimming, and climbing robots, have been developed inspired by living creatures. However, most of the reported bionic soft robots have only a single mode of motion, which limits their practical application. Herein, we report a fully 3D printed crawling and flipping soft robot using liquid metal incorporated liquid crystal elastomer (LM-LCE) composite as the actuator. With the application of voltage, liquid metal works as the conductive Joule heating material to induce the contraction of the LCE layer. The bending angle of the LM-LCE composite actuator highly depends on the applied voltage. We further demonstrate that the soft robot can exhibit distinct moving behaviors, such as crawling or flipping, by applying different voltages. The fully 3D printed LM-LCE composite structure provides a strategy for the fast construction of soft robots with diverse motion modes.

Keywords Liquid crystal elastomer; Liquid metal; Soft actuator; 3D printing

Citation: Yuan, L. X.; Liu, C. Y.; Yang, J. P.; Wang, Z. J. Soft crawling and flipping robots based on liquid metal-liquid crystal elastomer composites. *Chinese J. Polym. Sci.* **2025**, *43*, 588–596.

INTRODUCTION

Soft robots are made of soft active materials and have shown great potential, with high degrees of freedom, large deformations, and benign human-machine interactions. In the past decade, researchers have developed a variety of soft robots with diverse motion modes and functions by mimicking the deformation and motion of living organisms.[1–4] For example, inchworms achieve a crawling motion by alternating body contractions and stretching. Inspired by this, Yu and coworkers constructed a soft robot capable of simulating the crawling of inchworms, consisting of a deformable heater, sensor, and carbon black-liquid crystal elastomer composite material.[5] Inspired by the tubular feet of starfish, Cai and coworkers constructed a soft tubular actuator that could exhibit various deformation motions with multiple degrees of freedom (DOF).[6] In the past decades, diverse soft active materials have been employed to construct bioinspired soft robots, including shape memory polymers (SMPs),[7–10] hydrogels,[11–13] dielectric elastomers (DEs),[14,15] and liquid crystal elastomers (LCEs),[16–21] *etc*. Among these soft active materials, LCEs have attracted significant interest because of their large and reversible actuation strain and versatile and programmable actuation modes. The LCEs were fabricated by integrating liquid crystal mesogens with polymer networks. When heated above the nematic-isotropic phase transition temperature (T_i), the LCEs undergo macroscopic and anisotropic deformation. The deformation was fully reversible. Once cooled, the deformed LCEs recovered their initial shapes. This large and reversible deformation makes LCEs promising actuation materials for driving the locomotion of soft robots. The deformation behaviors of LCEs highly depend on the alignment of the mesogens inside, which can be programmed by different fabrication methods, such as mechanical stretching,[22–24] surface-enforced alignment,[25,26] and direct ink writing (DIW) printing techniques,[27–31] *etc*. The motion modes can be made complex and diverse by combining the LCE layers with different alignment patterns.

Different heating methods have been introduced to trigger the deformation of LCEs. Compared with conventional heating, electrothermal Joule heating can convert electric voltage to heat sequentially. To enable Joule heating, different electrothermal elements have been embedded into LCEs, including carbon nanotubes,[32] serpentine metallic wires,[33–35] and carbon black.[36,37] However, high electrical conductivity requires a high content of carbon nanotubes, making the LCEs hard and brittle. However, serpentine metallic wires would restrict the stretch ability of the entire structure owing to localized stiffness mismatches. Thus, new types

* Corresponding authors, E-mail: jyang@buaa.edu.cn (J.P.Y.)
E-mail: zhijianw@buaa.edu.cn (Z.J.W.)

Special Topic: Smart Elastomers and Actuators
Received October 30, 2024; Accepted November 24, 2024; Published online February 10, 2025

of soft electrothermal materials for LCE actuators are emerging. Liquid metals (LMs) are elemental metals or alloys with low melting points that exhibit unique physical and chemical properties, including excellent flexibility and high thermal and electrical conductivity.[38] LMs can be 3D printed into different patterns and are widely utilized as electrothermal elements in soft robots and flexible electronics.[39,40] For example, Majidi and coworkers reported flexible multifunctional composite materials based on LCEs and LMs as dispersions.[41] This composite combines sensing, mechanically stable conductive pathways, and active deformation, exhibiting multifunctional characteristics and application potential in sensing, actuation, circuits, and soft robots.

In addition to the crawling motion, the starfish can also turn their bodies over when they fall with tubular feet upside. However, it is difficult to realize such body-flipping motions in previously reported soft robots. This is because, to turn over the body, a massive shift of the center of gravity in the structure is needed, which is highly challenging for soft active materials and structural design. In this work, we report a starfish-inspired soft robot with crawling and flipping motion modes that was fully constructed by 3D printing. To construct an electrothermal actuator with multiple modes, an electrothermal LM layer was printed in the middle of the sandwich structure (Fig. 1a). The top and bottom layers were made from LCE layers with distinct actuation performances, which were printed by varying the printing path and parameters. The bending behavior of the sandwich structure can be adjusted by adjusting the applied voltage or the actuation performance of the top and bottom LCE layers. Owing to the large bending deformation, the LM-LCE composite actuator can undertake crawling and flipping modes as well as two distinct motion modes by simply varying the applied voltage.

EXPERIMENTAL

Materials

1,4-Bis-[4-(3-acryloyloxypropyloxy) benzoyloxy]-2-methylbenzene (RM257, 98%), 2,2-(ethylenedioxy) diethanethiol (EDDET, Aladdin, 97%), dipropylamine (DPA, Innochem, 99%), 2-hydroxy-4'-(2-hydroxyethoxy)-2-methylpropiophenone (I2959, Innochem, 98%), dichloromethane (CH_2Cl_2, Innochem, 99.5%), Gallium Indium eutectic (EGaIn, Ga:In=75.5:24.5, Aladdin), and alginic acid sodium salt (Innochem) were used as received without further purification.

Preparation of Printable LCE Ink

RM257 (10.301 g, 17.5 mmol) and the chain extender EDDET (2.735 g, 15 mmol) are dissolved in 30 mL of CH_2Cl_2. Then the

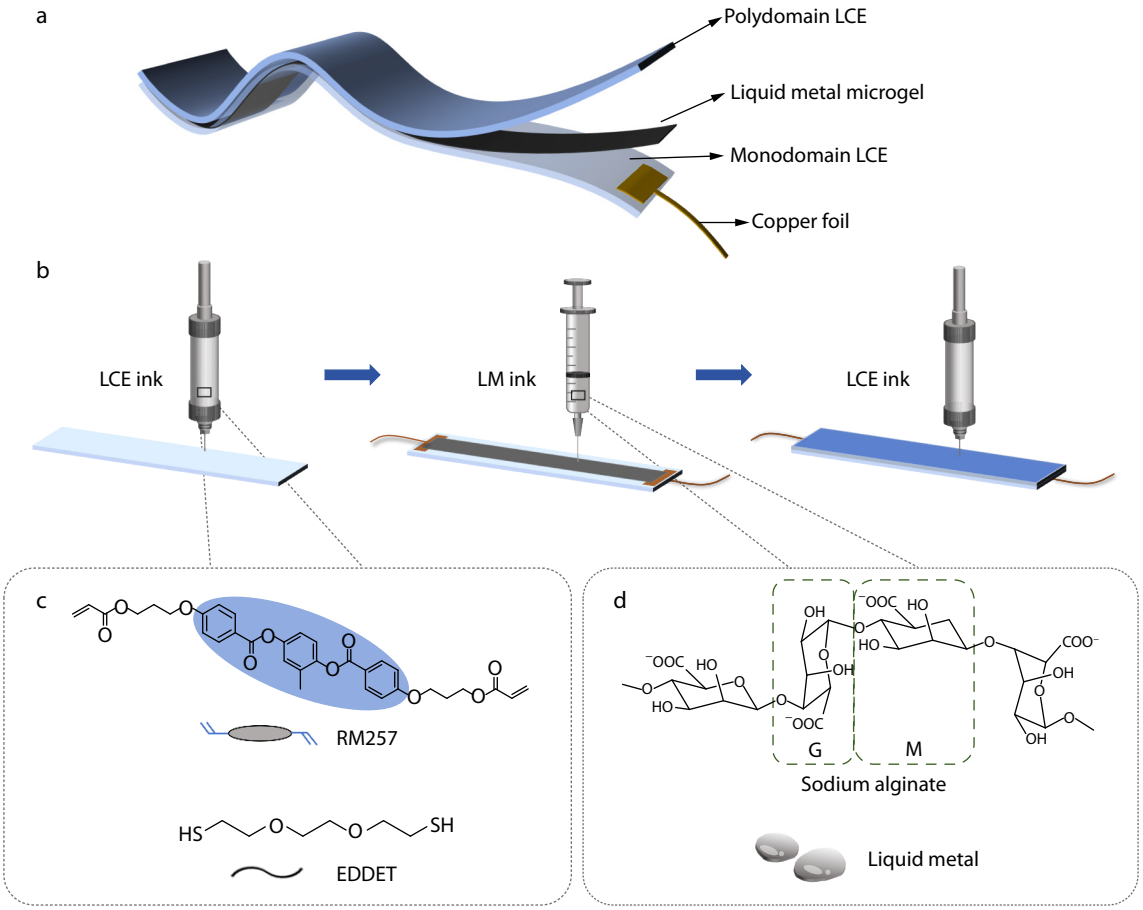

Fig. 1 Design and fabrication of electrothermal LM-LCE soft actuator. (a) Exploded view of the LM-LCE actuator consisting of LM layer sandwiched between a polydomain LCE layer and a monodomain LCE layer; (b) DIW printing of LM-LCE soft actuator; (c) Chemical structures of applied liquid crystalline (LC) monomers and dithiol chain extender in LCE ink; (d) Raw material for LM ink.

https://doi.org/10.1007/s10118-025-3276-z

catalyst DPA (0.125 g, 1.25 mmol) is added into the mixture and the mixture is stirred for 12 h at room temperature. The photoinitiator I2959 (0.067 g, 0.3 mmol) was added to the solution and stirred evenly. Finally, the mixture was placed in an oven at 80 °C for 24 h to evaporate the solvent completely. Thus, the LCE ink was obtained.

Preparation of Printable LM Ink

First, 4 wt% sodium alginate aqueous solution (4 g) was mixed with EGaIn (2 g), and the mixture was mechanically stirred for 20 min in a planetary mixer (ARE-310) at a speed of 2000 r/min. The resultant dispersion was further centrifuged at 3000 r/min for 8 min and the upper layer of the alginate solution was removed. Finally, the LM ink was obtained.

3D Printing of LM-LCE Actuator

First, the LCE ink was loaded into a steel syringe and placed in an oven at 80 °C for 12 h to remove bubbles. The bottom LCE layer was printed at 40 °C with a needle diameter of 0.84 mm, and printing speed of 2 mm/s. The LM layer was printed at room temperature with a needle diameter of 0.62 mm, and printing speed of 0.6 mm/s. The top LCE layer was printed at 140 °C and the diameter of the needle was 0.84 mm. LCE and LM layers were printed using a DIW 3D printer (Engine SR, Hyrel 3D).

Characterization

^{1}H-NMR spectroscopy measurements were conducted on an AV400M spectrometer at room temperature using chloroform-d ($CDCl_3$) as the solvent. Fourier-transform infrared (FTIR) spectra were recorded using a Nicolet 6700 spectrometer. The signal was recorded from 4000 cm^{-1} to 400 cm^{-1}. Thermogravimetric analysis (TGA) was performed on a Mettler TG-DSC 3+ instrument in a nitrogen atmosphere. The temperature range of the TGA measurements was from 25 °C to 800 °C, and the heating rate was set at 5 °C·min^{-1}. Differential scanning calorimetry (DSC) measurements were performed using a TA DSC2A-02163 instrument. The LCE ink and film were heated and cooled at a ramping rate of 10 °C·min^{-1} under nitrogen atmosphere. The DSC curve of the second heating run was used to remove the thermal history of the samples. Rheological characterization of the LCE ink was conducted using a Discovery DHR-2 Rheometer (TA Instruments), with a 25 mm steel Peltier plate and a 0.5 mm gap size. The shear rate ranges from 0.01 s^{-1} to 100 s^{-1} continuously. Polarized optical microscopy (POM) images were obtained using a 59XF-PC microscope. Wide-angle X-ray scattering (WAXS) experiments were conducted using an Xeuss 3.0 HR instrument (Xenocs). Data were collected at a distance of 900 nm from the detector (Pilatus 300 K) using an incident X-ray beam (30 W, 1.542 Å wavelength). Tensile tests of the LCEs were carried out on a universal material testing machine (WANCE, ETM504C) with a 100 N load cell. The samples were cut into rectangular shapes with dimensions of 10 mm × 30 mm. During the uniaxial tensile test, the strain rate was set to 0.2 min^{-1}. Optical images were captured using a NIKON Z5 camera.

RESULTS AND DISCUSSION

Preparation of Printable LCE Ink

The entire sandwich structure is constructed by the direct ink writing (DIW) 3D printing method, including the printing of LCE and LM (Fig. 1b). The bottom and top LCE layers are printed using the same ink and different printing parameters. The printable LCE ink is prepared according to previously reported procedures.[42] It consists of a liquid crystal oligomer that ends with polymerizable acrylate groups, which are synthesized from a reactive mesogenic monomer (RM257) and a dithiol chain extender (EDDET) *via* thiol-acrylate Michael addition (Fig. S1 in the electronic supplementary information, ESI). The degree of polymerization can be controlled by adjusting the ratio of RM257 to EDDET (Fig. 1c). First, the liquid crystal mesogen RM257 (10.301 g, 17.5 mmol) is dissolved in 30 mL of CH_2Cl_2, and the chain extender EDDET (2.735 g, 15 mmol) and catalyst dipropylamine (0.125 g, 1.25 mmol) are added. After stirring for 12 h at room temperature, photoinitiator I2959 (0.067 g, 0.3 mmol) is added to the mixture. Printable LCE ink is obtained after evaporating the solvent. The degree of polymerization of the oligomer ink is characterized by ^{1}H NMR spectroscopy (Fig. S2 in ESI). DP can be calculated as $3I(a)/(2I(b) + 2I(c) + 2I(d)) - 1 = 6.5$, where I is the integration of each peak, which is consistent with the feed ratio between the acrylate groups and thiol groups.

After extrusion from the printing nozzle, the liquid crystal mesogens in the oligomers are aligned along the printing path under shear stress. Then, the alignment of the liquid crystal mesogens is fixed by the formation of a polymer network in the presence of a photoinitiator and UV light. The desired alignment patterns and three-dimensional shapes can be created by programming the auxiliary software in a DIW 3D printer. With different alignment patterns, the LCE actuators exhibit various deformation modes, enabling the construction of soft robots with multiple modes.

Preparation of Printable Electrothermal LM Ink

A soft and stretchable electrothermal LM layer is printed between the two LCE layers. The LM printing ink is prepared using EGaIn (75.5% Ga and 24.5% In) and sodium alginate following previously reported procedures (Fig. 1d).[43] EGaIn is a typical LM material with excellent thermal conductivity, high flexibility, and high fluidity, with a low melting point of 15.7 °C and a high electrical conductivity of approximately 3.4×10^6 S·m^{-1}.[44] However, EGaIn alloys have low viscosity and high surface tension, and oxide films are spontaneously formed on their surfaces when EGaIn is exposed to air.[45] Thus, EGaIn gathers into a spherical shape instead of a continuous filament while being printed, making it difficult to print and adhere to the elastomer. To make the LM printable, we first mechanically mix EGaIn and sodium alginate aqueous solutions in a mass ratio of 2:1 to obtain the LM droplet dispersion by stirring. After mechanical stirring and centrifugation, the LM ink is in the bottom layer. The LM ink is obtained after removing the aqueous sodium alginate solution. By mixing EGaIn with sodium alginate, Ga is partially oxidized to Ga^{3+} ions. Ga^{3+} ions crosslink with sodium alginate to form microgel shells, enveloping the LM nanodroplets and forming a core-shell structure. Owing to this core-shell structure, the fluidity of the LM ink decreases and the adhesion between the LM ink and elastomer increases, making the LM ink printable.

3D Printing of the LM-LCE Actuator

Before printing the actuator, we characterize the thermal properties of the LCE ink by differential scanning calorimetry (DSC). The experimental results show that the LCE ink has a glass transition temperature (T_g) of −25.7 °C and a nematic-isotropic phase transition temperature (T_i) of 43.5 °C (Fig. 2a). After

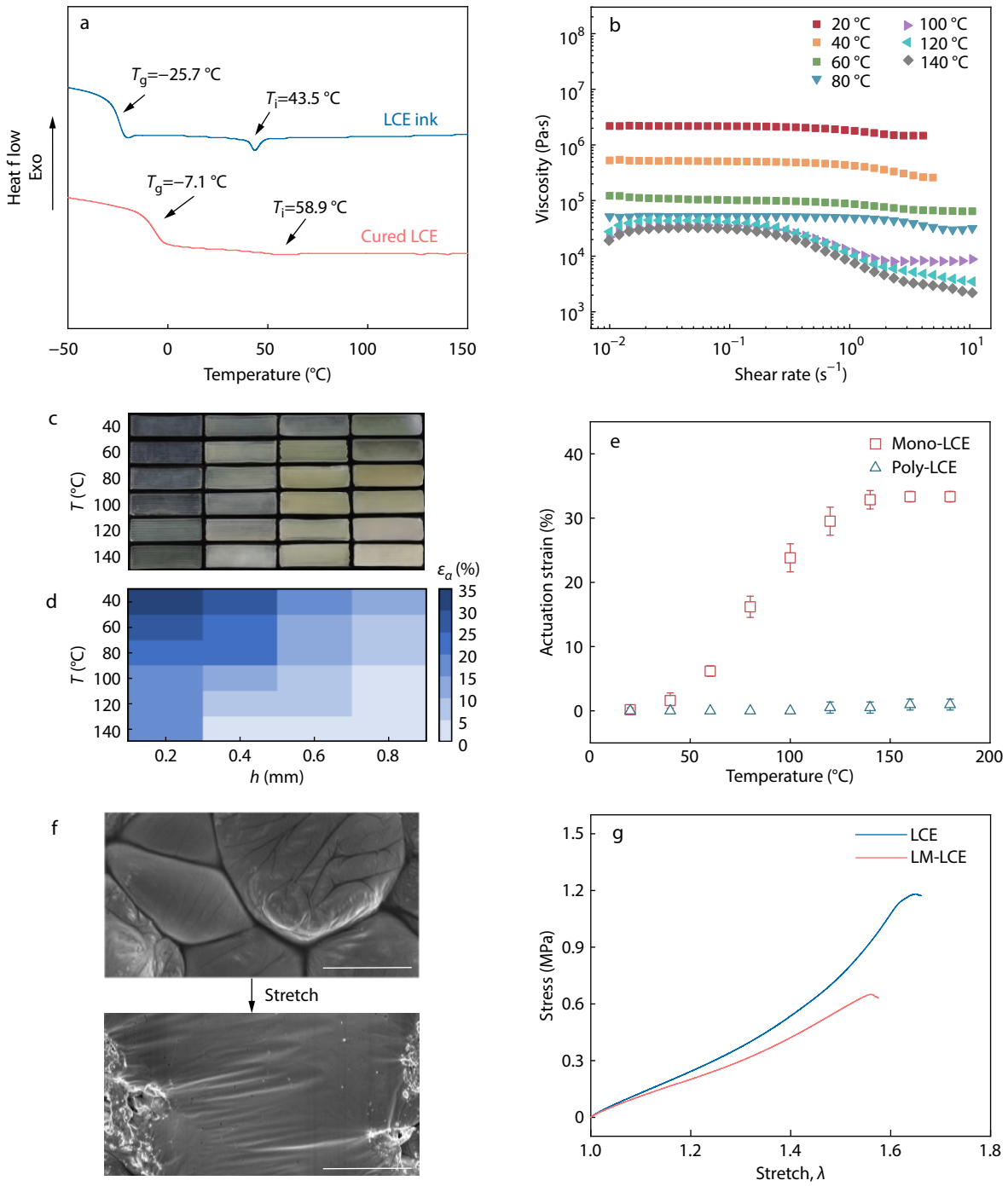

Fig. 2 DIW printing and properties of LCE and LM ink. (a) Differential scanning calorimetry (DSC) curves of LCE ink and cured LCE; (b) Viscosity curves of LCE ink with shear rate at different temperatures; (c) Optical photos and (d) actuation strain of printed LCE sheets at different printing temperatures *T* and gap sizes *h*. The printed sheet has a rectangular shape with a size of 30 mm × 10 mm; (e) Actuation strain of mono-LCE and poly-LCE at different temperatures; (f) Scanning electron microscope (SEM) images of LM layer surface before and after applying a light stress. Scale bars: 50 μm; (g) Uniaxial tensile test curves of LCE sheets and LM-LCE sheets printed by DIW method.

crosslinking under UV light, T_g and T_i increase to −7.1 °C and 58.9 °C, respectively. The thermal decomposition temperature (T_d) of the printed LCE is 327.9 °C, indicating that the LCEs can remain stable in our experimental temperature range, which is below 200 °C (Fig. S3 in ESI). We also use Fourier transform infrared (FTIR) spectroscopy to characterize the chemical structure evolution of the oligomer and cured LCE, and the results show that after the UV light-induced crosslinking reaction, the residual acrylates have been completely consumed (Fig. S4 in ESI). We further measure the viscosity of the LCE ink at various temperatures, which significantly affects the extrusion process during printing. As the temperature increases, the viscosity of

https://doi.org/10.1007/s10118-025-3276-z

the LCE ink decreases dramatically, varying by three orders of magnitude between 20 and 140 °C (Fig. 2b). At a temperature of 20 °C, the viscosity of the LCE ink is 10^6 Pa·s. With an increase in temperature, the viscosity of the LCE ink decreases drastically. When the temperature reaches 140 °C, the viscosity of the LCE ink decreases to 10^3 Pa·s. With lower viscosity, the LCE ink can be extruded smoothly.

It is well known that the actuation performance of printed LCEs can be adjusted by controlling the printing parameters, including *T* (printing temperature) and *h* (gap size, distance between the nozzle and plate). We explore the relationship between the actuation properties of the printed LCE films and different printing parameters. A series of LCE specimens are printed under different printing temperatures *T* (from 40 °C to 140 °C) and gap distances *h* (from 0.2 mm to 0.8 mm). It should be noted that the thickness of the printed LCE films is larger than the gap distance *h* because of the Barus effect. When *h* is set as 0.2 mm, the actual thickness of the LCE specimen is approximately 0.27 mm. And when *h* increases to 0.8 mm, the actual thickness increases to 1.11 mm. The actual thickness of the printed filament is found to have a linear relationship with the gap size (Fig. S5 in the ESI), which means that the actual thickness of the filament could be controlled by tuning the gap size.

LCE specimens printed under different conditions exhibites different appearances. As shown in Fig. 2(c), with increasing *T* and h, the transparency of the LCE films decreases. This is because the mesogens of the printed LCEs possess a better alignment under a lower printing temperature and smaller gap size, resulting in a more transparent appearance. We measure the reversible actuation strain of the crosslinked LCEs during cyclic heating and cooling processes. The actuation strain ε_a along the direction of the printing path is defined as $\varepsilon_a = \frac{L_0 - L}{L_0} \times 100\%$, where L_0, L are the lengths of the printed LCE films at the ambient temperature and 160 °C, respectively. When *h* is fixed, with an increase in *T*, the actuation strain of the LCE films decreases (Fig. 2d). Similarly, for a fixed *T*, when h increases, the actuation strain of the LCE films also decreases. When the printing temperature is increased, the mesogenic alignment can change from an ordered state after extrusion to a disordered state, leading to a polydomain state with a smaller actuation strain. When the gap size *h* is large, the shear force during the printing process decreases, which also leads to disordered mesogens and a decrease in the actuation strain. The experimental data are in consistent with those reported previously.[42]

The mesogen alignment in the printed LCE films is studied using wide-angle X-ray scattering (WAXS) and polarized optical microscopy (POM) (Fig. S6 in ESI). We print monodomain LCE films at 40 °C with an *h* of 0.2 mm, and printed polydomain LCE films at 140 °C with an *h* of 0.4 mm. These are denoted as mono-LCEs and poly-LCEs, respectively. The WAXS pattern of mono-LCE possesses a pair of arcs, whereas the pattern of poly-LCE is a ring, indicating that the former is a monodomain state and the latter is a polydomain state. The POM image shows a birefringence phenomenon for mono-LCE. The brightness changes when the polarizer is rotated by 45°. Nevertheless, for poly-LCE, the POM image remains dark, regardless of the rotation angle.

To construct an actuator with a large bending ability, the monodomain LCE layer printed at 40 °C with an *h* of 0.2 mm is utilized as bottom layer. The actuation strain of the monodomain LCE specimen increases gradually during heating, with a maximum contraction of 31.0% at 140 °C (Fig. 2e). Then, the electrothermal LM layer is printed on the monodomain LCE layer with a thickness of 0.2 mm, and the copper foils are connected to both ends of the LM layer (Fig. S7 in ESI). Scanning electron microscopy (SEM) images show that the LM layer changes from a core-shell structure to a continuous path after stretching, which is consistent with a previous report (Fig. 2f).[43] Lastly, the LCE ink, which is the same as the monodomain LCE, is utilized to print a polydomain LCE layer on the top as a passive layer. The polydomain LCE layer is printed at 140 °C with an *h* of 0.4 mm, which shows no actuation ability (Fig. S8 in ESI). At the interface of the printed LCE layers, covalent bonding is formed owing to the polymerization of the acrylate groups. Thus, the two LCE layers are firmly bonded together, and the LM layer is encapsulated to avoid leakage. Finally, a sandwich-structured actuator consisting of a monodomain LCE layer, an LM layer, and a polydomain LCE layer, is obtained.

We explore the mechanical properties of the LM-LCE actuators. Using a mechanical testing machine, we measure the stress-strain curves of the two-layer and three-layer structures (Fig. 2g). A tensile force is applied along the length direction, and the strain rate is 0.2 min^{-1}. The uniaxial tensile tests demonstrate that, compared to the LCE bilayer structure, the sandwich LM-LCE actuator exhibits a lower Young's modulus of 1.40 MPa due to the lower modulus of the LM layer.

Electrothermal Performance of the LM-LCE Actuators

Upon applying direct current (DC) voltage, the LM layer generates Joule heat, which increases the temperature of the overall actuator. When the temperature is higher than T_i, the nematic phase of the monodomain LCE changes to an isotropic phase, accompanied by a large contraction deformation, while the polydomain LCE layer maintains its initial shape, resulting in the whole sandwich structure bending towards the monodomain LCE layer (Fig. 3a). We gradually increase the applied constant voltage from 0.6 V to 1.6 V and measure the maximum surface temperature that the actuator can reach through the infrared thermometer. An LM-LCE sample with dimensions of 5 mm × 30 mm × 1 mm is used for testing. The thermal images of the LM-LCE actuators are shown in Fig. S9 (in ESI), and the relationship between the surface temperature and the applied voltage is plotted in Fig. 3(b). With an increase in the voltage, the maximum surface temperature also increases. It will reach 131.2 °C when a DC voltage of 1.5 V is applied. However, when the applied voltage is too high, the LM circuit may burn and disconnect. Therefore, the applied voltage should be maintained within an appropriate range.

We further measure the bending angle versus the applied voltage (Fig. 3c). The bending angle is defined as the angle between the tangent lines at both ends of the actuator. A clamp is placed on one end of the actuator to hang it upwards. When a constant DC voltage is applied, it overcomes gravity and undergoes a bending deformation. Under an applied DC voltage of 1.5 V, the actuator achieves a high-performance actuation within 90 s (Fig. 3d). The bending angle of the actuator increases with the applied voltage. It can reach

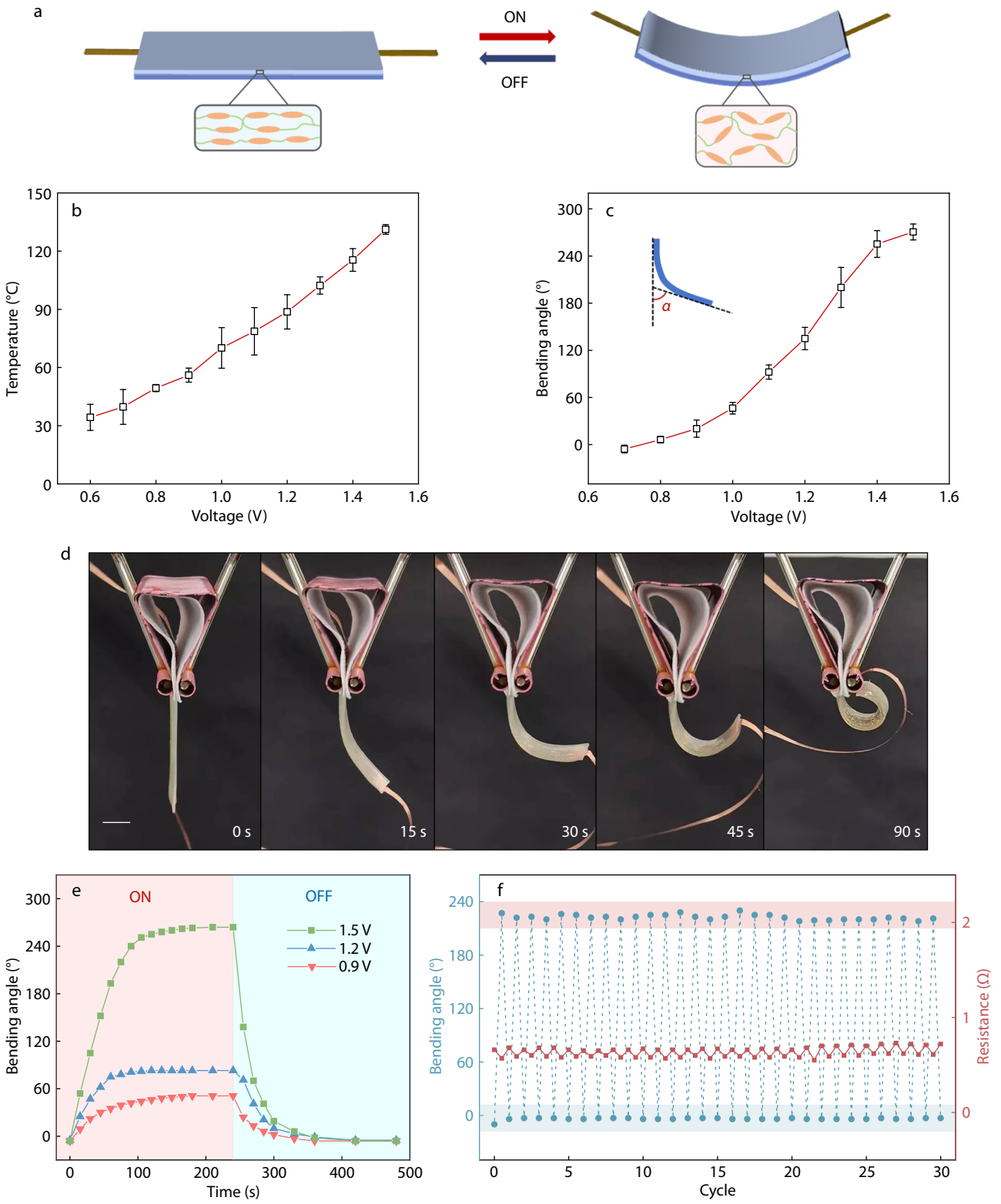

Fig. 3 Mechanical and electrical performance of the LM-LCE actuator. (a) Schematic illustration showing the bending deformation of LM-LCE actuator under a constant voltage; (b) Maximal temperature that LM-LCE actuator can reach as a function of different applied voltages; (c) Bending angle variations of LM-LCE actuator as a function of constant voltage; (d) Optical images of the bending deformation of LM-LCE actuator at different time upon applied voltage. Scale bar: 5 mm. (e) Bending angle variations of LM-LCE actuator as a function of time under different voltages of 0.9 V, 1.2 V, and 1.5 V; (f) Bending angle and electrical resistance variations of LM-LCE actuator during the power turn-on and turn-off cycle.

https://doi.org/10.1007/s10118-025-3276-z

270.1° when a voltage of 1.5 V is applied, thereby enabling the flipping mode of the LM-LCE actuator. When the voltage is switched off, the actuator recovers to its original vertical state.

We apply different voltages of 0.9, 1.2 and 1.5 V to the LM-LCE actuator and measure their bending angle, respectively (Fig. 3e). With an increase in the applied voltage, the response speed of the actuator accelerates, and the bending angle in the equilibrium state also increases. The bending angle can be stabilized at nearly 270° when a 1.5 V voltage is applied. After the power is turned off, the actuator eventually recovers to its initial state in 90 s. We further carry out a cyclic test of the LM-LCE actuator with on/off power. The interfaces of the upper and lower layers are bonded covalently bonded by polymerization of the residual acrylate groups in the oligomer ink. The LM-LCE actuator exhibits excellent long-term actuation stability. As shown in Fig. 3(f), there is no loss of the bending angle after 30 cycles. During 30 cycles, the electrical conductivity of the composite remains almost constant. In addition, under cyclic electrical stimuli and mechanical deformation, the multilayer structure of the actuator remains stable.

Electrothermal Soft Robot Based on LM-LCE Actuators

Based on the LM-LCE actuator, we design and construct a soft robot with two motion modes, crawling and flipping. The soft robot has the shape of an "X". It can be divided into the left and right halves. Half of them are three-layers, with the LM layer sandwiched between a polydomain LCE layer above and a monodomain LCE layer below. In this way, when a voltage is applied, the half with the sandwich structure bends downward, whereas the other half maintains the initial shape, enabling different motion modes of the soft robot.

First, we explore the crawling motion of a soft robot. To move forward rather than sliding in the initial place, we add Velcro to the middle part of the right legs to create friction between the right and left legs of the soft robot. A schematic of the crawling motion is shown in Fig. 4(a). When we apply an initial DC voltage of 2.2 V to the soft robot, the left half bends downward and moves forward, while the right half stays in place because of the larger friction. When the DC voltage is switched off, the curvature of the right half gradually decreases, with the right half arching, resulting in the right half moving forward with less friction. In this way, the soft robot can propel itself continuously and crawl rightward under intermittent voltages (Movie S1 in ESI). Photographs of the entire crawling process are shown in Fig. 4(b). We measure the crawling speed by recording the displacement of the right end point of the robot, as shown in Fig. 4(c). The crawl-

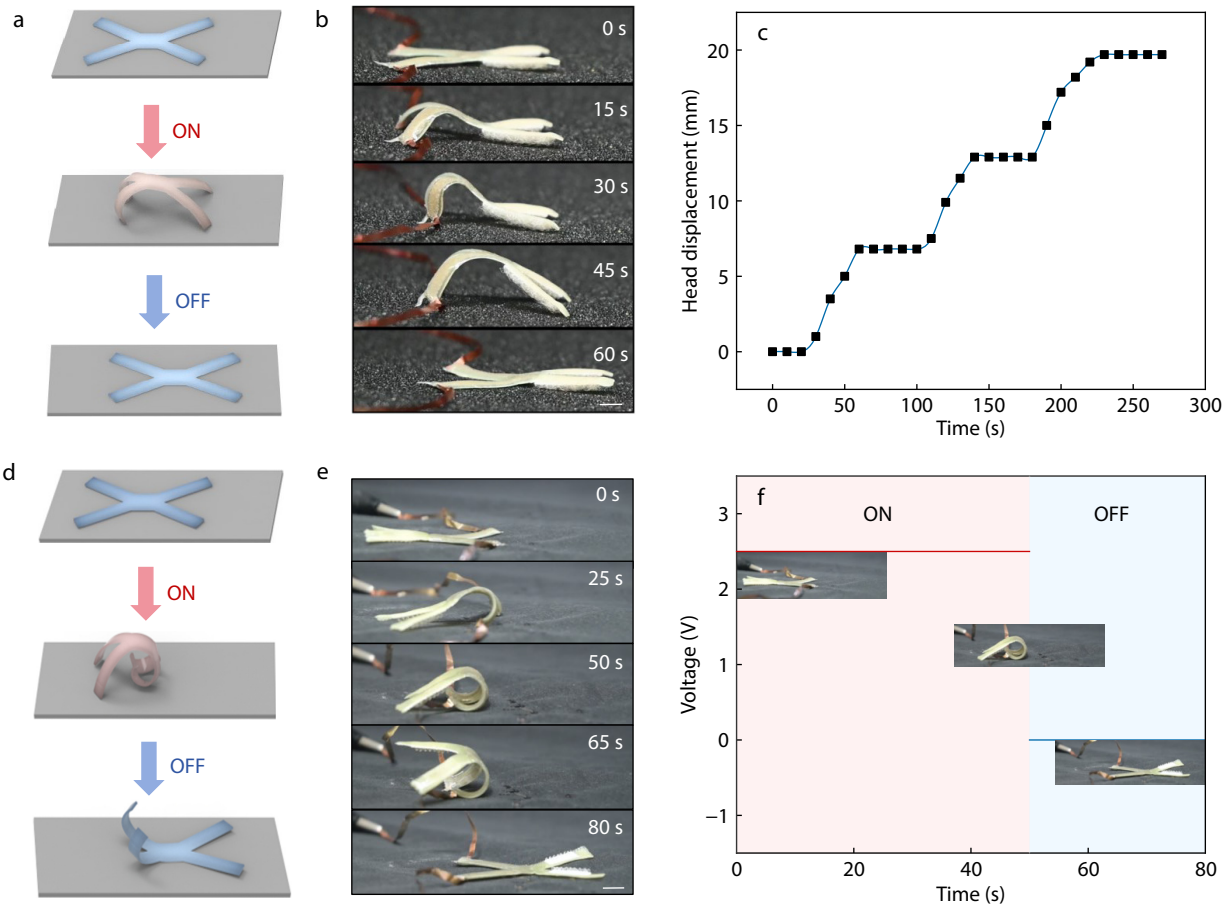

Fig. 4 Electrothermal induced crawling and flipping. (a) Schematic illustration showing the crawling process of LM-LCE soft robot; (b) Optical images showing the crawling process; (c) Head displacement of LM-LCE soft robot as a function of time in the crawling process; (d) Schematic illustration showing the flipping process of LM-LCE soft robot; (e) Optical images of the LM-LCE composite actuator in the flipping process. Scale bars: 10 mm. (f) The voltage applied at different time periods in the flipping process. Insert pictures: the LM-LCE actuator at different time.

https://doi.org/10.1007/s10118-025-3276-z

ing speed can reach 6.14 mm·min^{-1}, and the displacement of the robot at each step is approximately 0.13 body length.

In addition, we explore the flipping motion of a soft robot attached to Velcro. In this mode, we actuate the right half with a large voltage. As shown in Figs. 4(d)–4(f), we apply a DC voltage of 2.5 V, and the right half of the robot bends downward significantly. The bending angle of the right half continues to increase, and the center of gravity of the structure increases. After maintaining the power for 50 s, the structure loses balance and flips over. After the DC voltage being switched off for 30 s, the entire structure is restored to a flat state (Movie S2 in the ESI). In summary, the soft robot can realize two motion modes of crawling and flipping by tuning the applied voltage.

CONCLUSIONS

In conclusion, we develop an electrothermal LM-LCE actuator with full 3D printing that can perform crawling and flipping motions with different applied voltages. The printing inks of both the LCE and LM are studied in detail. The actuation performance of the LCE composite actuator could be adjusted by tuning the printing parameters. The incorporation of the LM layer enables the Joule heating of the composite actuator. The bending angle varies with the application of different voltages, enabling different motion modes. We believe that this study provides a convenient method for constructing soft robots with multiple motion modes.

Conflict of Interests

The authors declare no interest conflict.

Electronic Supplementary Information

Electronic supplementary information (ESI) is available free of charge in the online version of this article at http://doi.org/10.1007/s10118-025-3276-z.

Data Availability Statement

The data supporting the findings of this study are available from the corresponding author upon reasonable request. The author's contact information: zhijianw@buaa.edu.cn.

ACKNOWLEDGMENTS

This work was financially supported by the National Key Research and Development Program of China (No. 2023YFB3812500), the National Natural Science Foundation of China (No. 52105003) and Beijing Municipal Natural Science Foundation (No. 2222058), and Fundamental Research Funds for the Central Universities (No. YWF-22-K-101).

REFERENCES

1 Lin, H. T.; Leisk, G. G.; Trimmer, B. GoQBot: a caterpillar-inspired soft-bodied rolling robot. *Bioinspir. Biomim.* **2011**, *6*, 026007.
2 Wani, O. M.; Zeng, H.; Priimagi, A. A light-driven artificial flytrap. *Nat. Commun.* **2017**, *8*, 15546.
3 Wehner, M.; Truby, R. L.; Fitzgerald, D. J.; Mosadegh, B.; Whitesides, G. M.; Lewis, J. A.; Wood, R. J. An integrated design and fabrication strategy for entirely soft, autonomous robots. *Nature* **2016**, *536*, 451–455.
4 Wang, Z. J.; Li, K.; He, Q. G.; Cai, S. Q. A light-powered ultralight tensegrity robot with high deformability and load capacity. *Adv. Mater.* **2019**, *31*, 1806849.
5 Wang, C. J.; Sim, K.; Chen, J.; Kim, H.; Rao, Z. Y.; Li, Y. H.; Chen, W. Q.; Song, J. Z.; Verduzco, R.; Yu, C. J. Soft ultrathin electronics innervated adaptive fully soft robots. *Adv. Mater.* **2018**, *30*, 1706695.
6 He, Q. G.; Wang, Z. J.; Wang, Y.; Minori, A.; Tolley, M. T.; Cai, S. Q. Electrically controlled liquid crystal elastomer-based soft tubular actuator with multimodal actuation. *Sci. Adv.* **2019**, *5*, eaax5746.
7 Lendlein, A.; Langer, R. Biodegradable, elastic shape-memory polymers for potential biomedical applications. *Science* **2002**, *296*, 1673–1676.
8 Lendlein, A.; Gould, O. E. C. Reprogrammable recovery and actuation behaviour of shape-memory polymers. *Nat. Rev. Mater.* **2019**, *4*, 116–133.
9 Behl, M.; Kratz, K.; Zotzmann, J.; Nöchel, U.; Lendlein, A. Reversible bidirectional shape-memory polymers. *Adv. Mater.* **2013**, *25*, 4466–4469.
10 Zhang, X.; Zhu, C. Y.; Xu, B.; Qin, L.; Wei, J.; Yu, Y. L. Rapid, localized, and athermal shape memory performance triggered by photoswitchable glass transition temperature. *ACS Appl. Mater. Interfaces* **2019**, *11*, 46212–46218.
11 Sun, J.-Y.; Zhao, X.; Illeperuma, W. R. K.; Chaudhuri, O.; Oh, K. H.; Mooney, D. J.; Vlassak, J. J.; Suo, Z. Highly stretchable and tough hydrogels. *Nature* **2012**, *489*, 133–136.
12 Yuk, H.; Lin, S. T.; Ma, C.; Takaffoli, M.; Fang, N. X.; Zhao, X. H. Hydraulic hydrogel actuators and robots optically and sonically camouflaged in water. *Nat. Commun.* **2017**, *8*, 14230.
13 Lee, Y.; Song, W. J.; Sun, J. Y. Hydrogel soft robotics. *Mater. Today Phys.* **2020**, *15*, 100258.
14 Li, G. R.; Chen, X. P.; Zhou, F. H.; Liang, Y. M.; Xiao, Y. H.; Cao, X.; Zhang, Z.; Zhang, M. Q.; Wu, B. S.; Yin, S. Y. Self-powered soft robot in the Mariana Trench. *Nature* **2021**, *591*, 7848, 66-71.
15 Gupta, U.; Qin, L.; Wang, Y. Z.; Godaba, H.; Zhu, J. Soft robots based on dielectric elastomer actuators: a review. *Smart Mater. Struct.* **2019**, *28*, 103002.
16 Saed, M. O.; Torbati, A. H.; Starr, C. A.; Visvanathan, R.; Clark, N. A.; Yakacki, C. M. Thiol-acrylate main-chain liquid-crystalline elastomers with tunable thermomechanical properties and actuation strain. *J. Polym. Sci., Part B: Polym. Phys.* **2017**, *55*, 157–168.
17 White, T. J.; Broer, D. J. Programmable and adaptive mechanics with liquid crystal polymer networks and elastomers. *Nat. Mater.* **2015**, *14*, 1087–1098.
18 Herbert, K. M.; Fowler, H. E.; McCracken, J. M.; Schlafmann, K. R.; Koch, J. A.; White, T. J. Synthesis and alignment of liquid crystalline elastomers. *Nat. Rev. Mater.* **2022**, *7*, 23–38.
19 Boothby, J. M.; Gagnon, J. C.; McDowell, E.; Van Volkenburg, T.; Currano, L.; Xia, Z. Y. An untethered soft robot based on liquid crystal elastomers. *Soft Robot.* **2022**, *9*, 154–162.
20 Liu, C. Y.; Li, K.; Yu, X. Z.; Yang, J. P.; Wang, Z. J. A multimodal self-propelling tensegrity structure. *Adv. Mater.* **2024**, *36*, 2314093.
21 He, Q. G.; Wang, Z. J.; Wang, Y.; Wang, Z. J.; Li, C. H.; Annapooranan, R.; Zeng, J.; Chen, R. K.; Cai, S. Q. Electrospun liquid crystal elastomer microfiber actuator. *Sci. Robot.* **2021**, *6*, eabi9704.
22 Yakacki, C. M.; Saed, M.; Nair, D. P.; Gong, T.; Reed, S. M.; Bowman,

C. N. Tailorable and programmable liquid-crystalline elastomers using a two-stage thiol-acrylate reaction. *RSC Adv.* **2015**, *5*, 18997–19001.
23 Barnes, M.; Verduzco, R. Direct shape programming of liquid crystal elastomers. *Soft Matter* **2019**, *15*, 870–879.
24 Song, C. J.; Zhang, Y. H.; Bao, J. Y.; Wang, Z. Z.; Zhang, L. Y.; Sun, J.; Lan, R. C.; Yu, Z.; Zhu, S. Q.; Yang, H. Light-responsive programmable shape-memory soft actuator based on liquid crystalline polymer/polyurethane network. *Adv. Funct. Mater.* **2023**, *33*, 2213771.
25 Zeng, H.; Wani, O. M.; Wasylczyk, P.; Kaczmarek, R.; Priimagi, A. Self-regulating iris based on light-actuated liquid crystal elastomer. *Adv. Mater.* **2017**, *29*, 1701814.
26 Kowalski, B. A.; Tondiglia, V. P.; Guin, T.; White, T. J. Voxel resolution in the directed self-assembly of liquid crystal polymer networks and elastomers. *Soft Matter* **2017**, *13*, 4335–4340.
27 Kotikian, A.; Truby, R. L.; Boley, J. W.; White, T. J.; Lewis, J. A. 3D printing of liquid crystal elastomeric actuators with spatially programed nematic order. *Adv. Mater.* **2018**, *30*, 1706164.
28 Davidson, E. C.; Kotikian, A.; Li, S. C.; Aizenberg, J.; Lewis, J. A. 3D printable and reconfigurable liquid crystal elastomers with light-induced shape memory *via* dynamic bond exchange. *Adv. Mater.* **2020**, *32*, 1905682.
29 Roach, D. J.; Kuang, X.; Yuan, C.; Chen, K. J.; Qi, H. J. Novel ink for ambient condition printing of liquid crystal elastomers for 4D printing. *Smart Mater. Struct.* **2018**, *27*, 125011.
30 Ambulo, C. P.; Burroughs, J. J.; Boothby, J. M.; Kim, H.; Shankar, M. R.; Ware, T. H. Four-dimensional printing of liquid crystal elastomers. *ACS Appl. Mater. Interfaces* **2017**, *9*, 37332–37339.
31 Mistry, D.; Traugutt, N. A.; Sanborn, B.; Volpe, R. H.; Chatham, L. S.; Zhou, R.; Song, B.; Yu, K.; Long, K. N.; Yakacki, C. M. Soft elasticity optimises dissipation in 3D-printed liquid crystal elastomers. *Nat. Commun.* **2021**, *12*, 6677.
32 Kim, H.; Lee, J. A.; Ambulo, C. P.; Lee, H.; Kim, S. H.; Naik, V. V.; Haines, C. S.; Aliev, A. E.; Ovalle-Robles, R.; Baughman, R. H. Intelligently actuating liquid crystal elastomer-carbon nanotube composites. *Adv. Funct. Mater.* **2019**, *29*, 1905063.
33 Xiao, Y. Y.; Jiang, Z. C.; Tong, X.; Zhao, Y. Biomimetic locomotion of electrically powered "Janus" soft robots using a liquid crystal polymer. *Adv. Mater.* **2019**, *31*, 1903452.
34 Zhao, L. M.; Tian, H. M.; Liu, H. R.; Zhang, W. T.; Zhao, F. B.; Song, X. W.; Shao, J. Y. Bio-inspired soft-rigid hybrid smart artificial muscle based on liquid crystal elastomer and helical metal wire. *Small* **2023**, *19*, 2206342.
35 Pang, W. B.; Xu, S. W.; Wu, J.; Bo, R. H.; Jin, T. Q.; Xiao, Y.; Liu, Z.; Zhang, F.; Cheng, X.; Bai, K. A soft microrobot with highly deformable 3D actuators for climbing and transitioning complex surfaces. *Proc. Natl. Acad. Sci.* **2022**, *119*, e2215028119.
36 Wang, M.; Cheng, Z. W.; Zuo, B.; Chen, X. M.; Huang, S.; Yang, H. Liquid crystal elastomer electric locomotives. *ACS Macro Lett.* **2020**, *9*, 860–865.
37 Min, J. Y.; Wu, Z. X.; Zhang, W.; Liu, Y. J.; Luo, D. Intelligent liquid crystal elastomer actuators with high mechanical strength, self-sensing, and automatic control. *Adv. Sensor Res.* **2024**, *3*, 2300117.
38 Chen, S.; Zhao, R. Q.; Sun, X. Y.; Wang, H. Z.; Li, L.; Liu, J. Toxicity and biocompatibility of liquid metals. *Adv. Healthc. Mater.* **2023**, *12*, 2201924.
39 Wang, X. L.; Liu, J. Recent advancements in liquid metal flexible printed electronics: properties, technologies, and applications. *Micromachines* **2016**, *7*, 206.
40 Neumann, T. V.; Dickey, M. D. Liquid metal direct write and 3D printing: a review. *Adv. Mater. Technol.* **2020**, *5*, 2000070.
41 Ford, M. J.; Ambulo, C. P.; Kent, T. A.; Markvicka, E. J.; Pan, C. F.; Malen, J.; Ware, T. H.; Majidi, C. A multifunctional shape-morphing elastomer with liquid metal inclusions. *Proc. Natl. Acad. Sci.* **2019**, *116*, 21438–21444.
42 Wang, Z. J.; Wang, Z. J.; Zheng, Y.; He, Q. G.; Wang, Y.; Cai, S. Q. Three-dimensional printing of functionally graded liquid crystal elastomer. *Sci. Adv.* **2020**, *6*, eabc0034.
43 Wu, P. C.; Fu, J. Z.; Xu, Y. T.; He, Y. Liquid metal microgels for three-dimensional printing of smart electronic clothes. *ACS Appl. Mater. Interfaces* **2022**, *14*, 13458–13467.
44 Zhao, Z.; Soni, S.; Lee, T.; Nijhuis, C. A.; Xiang, D. Smart eutectic gallium-indium: from properties to applications. *Adv. Mater.* **2023**, *35*, 2203391.
45 Liu, T. Y.; Sen, P.; Kim, C. Characterization of nontoxic liquid-metal alloy Galinstan for applications in microdevices. *J. Microelectromech. Syst.* **2012**, *21*, 443–450.

https://doi.org/10.1007/s10118-025-3276-z